Earth and Planetary Science Letters 510 (2019) 64–72

Contents lists available at ScienceDirect

Earth and Planetary Science Letters

www.elsevier.com/locate/epsl

Hydrothermal scavenging of ^{230}Th on the Southern East Pacific Rise during the last deglaciation

David C. Lund [a,*], Frank J. Pavia [b], Emily I. Seeley [a], Sarah E. McCart [a], Patrick A. Rafter [c], Kenneth A. Farley [d], Paul D. Asimow [d], Robert F. Anderson [b]

[a] Department of Marine Sciences, University of Connecticut, United States of America
[b] Lamont Doherty Earth Observatory, Columbia University, United States of America
[c] KECK Carbon Cycle Laboratory, University of California, Irvine, United States of America
[d] Division of Geological and Planetary Sciences, California Institute of Technology, United States of America

ARTICLE INFO

Article history:
Received 28 August 2018
Received in revised form 23 December 2018
Accepted 28 December 2018
Available online xxxx
Editor: D. Vance

Keywords:
230-Thorium
hydrothermal scavenging
glacial–interglacial
East Pacific Rise
231-Protactinium

ABSTRACT

Thorium-230 (^{230}Th) is a fundamental tool for estimating sediment fluxes in the open ocean. Because ^{230}Th is rapidly scavenged by particles falling through the water column, the flux of ^{230}Th to underlying sediments is typically equal to its water column production rate. However, recent surveys suggest hydrothermal plumes are unusually efficient scavengers of ^{230}Th. Here we show that hydrothermal scavenging on the Southern East Pacific Rise (SEPR) resulted in ^{230}Th fluxes several times higher than the water column production rate during the last deglaciation. Elevated fluxes likely require diffusive transport of dissolved ^{230}Th from the ridge flanks towards the ridge crest. Depending on the length-scale of ^{230}Th transport, the resulting deficits in ^{230}Th may yield overestimates of sediment flux to ridge flank sediments. We also show that Fe fluxes at 19°S on the SEPR lag those at 11°S and 6°S by several thousand years, inconsistent with a signal driven by changes in deep water pH and oxygen levels. Instead, variable hydrothermal activity is the simplest explanation of the observed signals in the Pacific, Indian, and Atlantic basins.

1. Introduction

Estimates of sediment flux are an essential component of oceanographic research, forming the basis for long-term estimates of biological export production (Kienast et al., 2007; Anderson et al., 2009), aeolian dust flux (Albani et al., 2015; McGee et al., 2016), and mid-ocean ridge hydrothermal activity (Middleton et al., 2016; Costa et al., 2017). One of the most common methods for estimating sediment flux is ^{230}Th-normalization. ^{230}Th is produced by radioactive decay of ^{234}U, which is soluble in seawater and has a long oceanic residence time. In contrast, dissolved ^{230}Th is readily scavenged by particles falling through the water column and its residence time is therefore relatively short. As a result, the flux of ^{230}Th to the seafloor is typically equal to its production rate by ^{234}U decay, which is constant and can be easily quantified (Bacon and Anderson, 1982; Henderson et al., 1999). The measured sedimentary ^{230}Th activity, once corrected for decay since deposition, in situ production, and detrital sources, therefore reflects the accumulation of sediment on the seafloor (Francois et al., 2004).

While the assumption of constant ^{230}Th flux generally holds in the open ocean, areas of anomalously high particle fallout along ocean boundaries yield ^{230}Th fluxes in excess of the water column production rate. In these so-called boundary scavenging regions, rapid ^{230}Th removal creates concentration gradients that drive lateral diffusion of ^{230}Th towards areas of high particle flux (Bacon, 1988; Bruland and Lohan, 2003). Similar ^{230}Th concentration gradients are found near mid-ocean ridges, where particle-laden hydrothermal plumes scavenge ^{230}Th from the water column (German et al., 2002; Hayes et al., 2015a; Pavia et al., 2018). The bulk distribution coefficient (K_d) of ^{230}Th for hydrothermal particles, defined as the activity per gram of particles divided by the activity per gram of seawater, is an order of magnitude higher than other sedimentary components such as calcium carbonate, organic matter, and continental detritus (Pavia et al., 2018; Anderson et al., 1983; Hayes et al., 2015b). Results from the GEOTRACES program indicate that hydrothermal scavenging creates deficits in dissolved ^{230}Th near the Mid-Atlantic Ridge (MAR) (Hayes et al., 2015a) and Southern East Pacific Rise (SEPR). In the case of the SEPR, elevated metal concentrations and dissolved ^{230}Th deficits

* Corresponding author.
E-mail address: david.lund@uconn.edu (D.C. Lund).

https://doi.org/10.1016/j.epsl.2018.12.037
0012-821X/

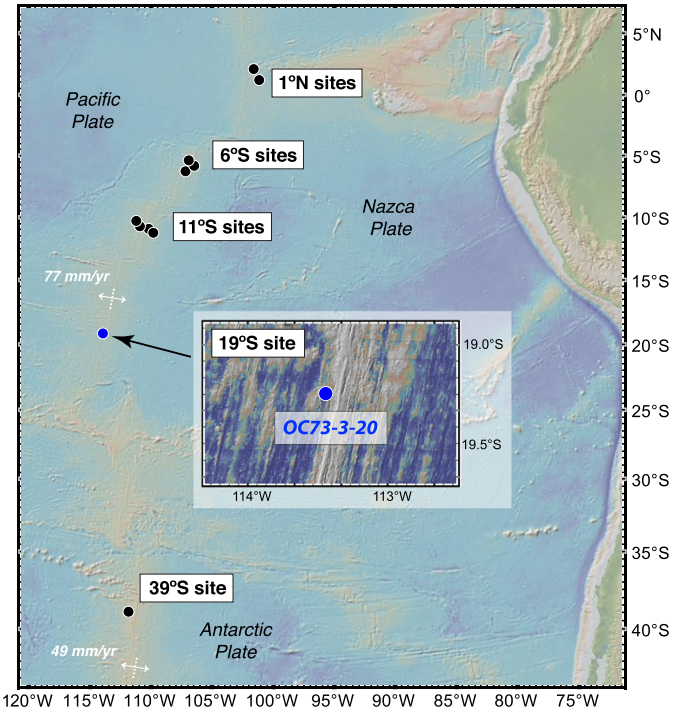

Fig. 1. Bathymetry in the vicinity of core OC73-3-20 (19.3°S, 113.6°W, 3081 m water depth). The core is located approximately 8 km west of the SEPR axis. The half-spreading rate along this section of the SEPR is 77 mm/yr (http://www.ldeo.columbia.edu/users/menke /plates.html). Also shown are the core locations at 1°N (Frank et al., 1994), 6°S (Lund et al., 2016), 11°S (Lund et al., 2016), and 39°S (Lund et al., 2018). The water depths for all cores range from 3000 to 3200 m, with the exception of KLH068 and KLH093 at 1°N (2870 m and 3260 m, respectively) and OC170-26-159 at 39°S (2750 m). Map generated using GeoMapApp (Ryan et al., 2009).

extend up to ~4000 km west of the ridge axis (Lopez et al., 2015; Resing et al., 2015; Pavia et al., 2018). Thus, hydrothermal plumes may effectively act as boundary scavenging locations in the open ocean, where it is typically assumed that such processes are negligible (German et al., 2002).

The SEPR has the fastest spreading rate and highest magmatic budget of any mid-ocean ridge on Earth (Baker and German, 2004). As a result, the SEPR is characterized by extensive hydrothermal plume coverage from 10°S to 30°S (Beaulieu et al., 2013), the fallout from which yields metal rich sediments spanning hundreds of kilometers on either side of the ridge axis (Dymond, 1981). Given that hydrothermal Fe oxyhydroxides and Mn oxides readily scavenge dissolved ^{230}Th, the flux of ^{230}Th to ridge-crest SEPR sediments is likely elevated relative to the water column production rate. While hydrothermal scavenging is known to yield anomalously high ^{230}Th fluxes within a few hundred meters of active vents on the northern EPR (German et al., 2002), estimates of ^{230}Th scavenging on the SEPR remain poorly constrained due to a lack of independent flux data. Furthermore, long-term variations in the scavenging of ^{230}Th remain unknown, despite evidence for variations in hydrothermal activity on the SEPR during the late Quaternary (Lund et al., 2016).

Here we evaluate hydrothermal scavenging of ^{230}Th using a record of metal fluxes from the super-fast section of the SEPR (>75 mm/yr half spreading rate). The core (OC73-3-20; 19.25°S, 113.58°W, 3081 m water depth) is located ~8 km west of the ridge axis (Fig. 1). We also present ^{230}Th results for two additional cores at 6°S and 11°S to characterize scavenging on multiple sections of the SEPR. We estimate ^{230}Th fluxes using the ^{3}He-normalization technique, which for the first time allows for reconstruction of ^{230}Th fluxes in a ridge flank setting on glacial–interglacial timescales. We show that hydrothermal scavenging resulted in anomalous fluxes of ^{230}Th to the SEPR axis at 6°S, 11°S, and 19°S and then discuss the implications of our results for ^{230}Th-normalization at the SEPR and other ridge locations. Additionally, we use the results from 19°S, combined with updated records from 6°S and 11°S, to demonstrate that variations in hydrothermal activity, rather than iron oxidation rate, are the most likely driver of the observed metal flux signals.

2. Results

Oxygen isotope and metal flux records for core OC73-3-20 are shown in Fig. 2. The oxygen isotope time series outlines the expected pattern for the past 30 kyr, including the Last Glacial Maximum (LGM) (~26 to 18 kyr BP) (Clark et al., 2009), deglaciation (18 to 8 kyr BP) (Fleming et al., 1998), and Holocene (Fig. 2a). At 19°S, Fe, Mn, and As fluxes were low from 40 to 15 kyr BP, peaked late in the deglaciation (13 to 10 kyr BP), and then returned to background levels during the Holocene (Fig. 2b–d). A similar pattern holds for Cu, Zn, and V (see Supplementary Material).

The covariation between Fe and other metals indicates that hydrothermal plume fallout is the primary source of metals to the core site. The highest correlation occurs for Fe/As and Fe/V ($r^2 = 0.99$), consistent with scavenging of these elements from seawater by colloidal ferrihydrite (Fig. S5) (Dunk and Mills, 2006). Similar down-core patterns in Fe/Cu and Fe/V imply that Cu is also associated with Fe-oxyhydroxides (Fig. S6), most likely via co-precipitation (Martínez and McBride, 1998; Savenko, 2001). While Cu is often associated with iron sulfides in hydrothermal settings, sulfide formation typically occurs very close to the vent site, with most of the associated deposition occurring during the buoyant plume phase (Rudnicki and Elderfield, 1993; German et al., 2002; German and Seyfried, 2014). The relatively low Fe/Mn ratio in OC73-3-20 (3.3 ± 0.4; 1σ) is inconsistent with the presence of iron sulfides because they typically lack appreciable amounts of Mn (German and Seyfried, 2014). Sulfide-rich plume particles collected in near-field sediment traps have Fe/Mn ratios exceeding 150 (German et al., 2002; Dymond and Roth, 1988; Khripounoff and Alberic, 1991). The strong correlation between Fe and Mn ($r^2 = 0.92$) in OC73-3-20 (Fig. S5) is most likely due to precipitation of Fe and Mn oxides from aged neutrally-buoyant hydrothermal plumes (Lilley et al., 1995). The mean Fe/Mn ratio is similar to that of metalliferous sediments at multiple ridge-flank locations on the SEPR (Dymond, 1981; Marchig et al., 1986; Shimmield and Price, 1988; Dunk and Mills, 2006). Additionally, the small down-core variations in Fe/Mn imply there has been little diagenetic remobilization of Mn at 19°S, similar to the pattern observed at 6°S and 11°S (Lund et al., 2016).

Background Fe and Mn fluxes at 19°S (~50 $\mu g\,cm^{-2}\,yr^{-1}$ and 15 $\mu g\,cm^{-2}\,yr^{-1}$, respectively) are ~5× higher than the other SEPR sites (Fig. 2). The deglacial signal at 19°S is also larger than the signals at 6°S and 11°S. Higher fluxes at 19°S are likely due to the proximity of the core site to the SEPR and elevated hydrothermal plume incidence in this region (Beaulieu et al., 2013). Core OC73-3-20 is located 8 km off-axis, while the 11°S and 6°S sites are located 15 km and 28 km off-axis, respectively (Lund et al., 2016). The timing of deglacial metal flux anomalies also varies between sites; at 19°S, the initial increase occurred at ~12 kyr BP, compared to 14–15 kyr BP at 6°S and 17–18 kyr BP at 11°S (Fig. 2). Thus, the metal flux maxima at 19°S lag those at 11°S and 6°S by 2–5 kyr (see Supplementary Material). The time offset is larger than the uncertainty for individual control points, which have a typical error of ±0.3 kyr (1σ) (Tables S2–S4).

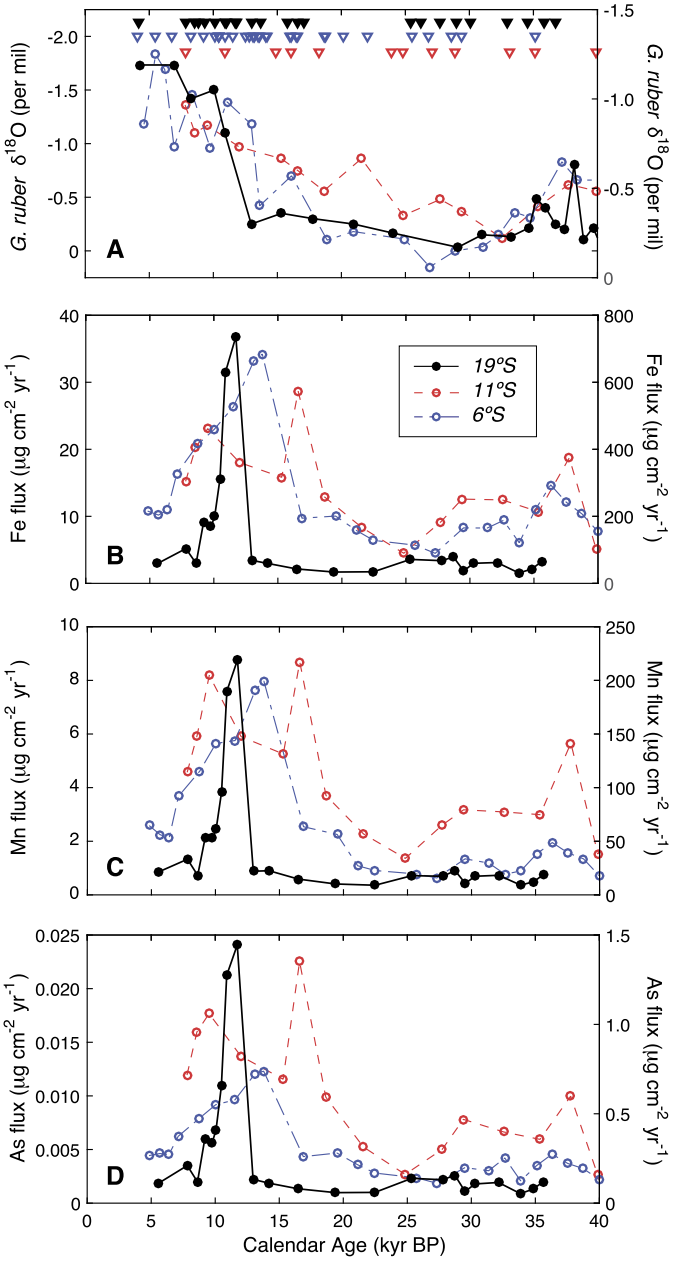

Fig. 2. Oxygen isotope and ^{3}He-normalized flux results for Fe, Mn, and As at three EPR sites, including 19°S (OC73-3-20; solid lines), 11°S (Y71-07-49; dashed lines) and 6°S (Y71-09-106; dash-dot lines). In all four panels, data for the 19°S site are plotted on the right-hand *y*-axis, whereas data from 6°S and 11°S are plotted on the left-hand *y*-axis. A) Planktonic (*G. ruber*) δ^{18}O (circles) and radiocarbon ages (triangles) for each core, B) Fe fluxes, C) Mn fluxes, and D) As fluxes. Both Fe and Mn fluxes have been corrected for detrital inputs (see Methods). Fluxes at 19°S lag those at 6°S and 11°S by 3–5 kyr. The records from 6°S and 11°S were published originally in (Lund et al., 2016) and are presented here with updated age models for comparison to the 19°S results (see Methods).

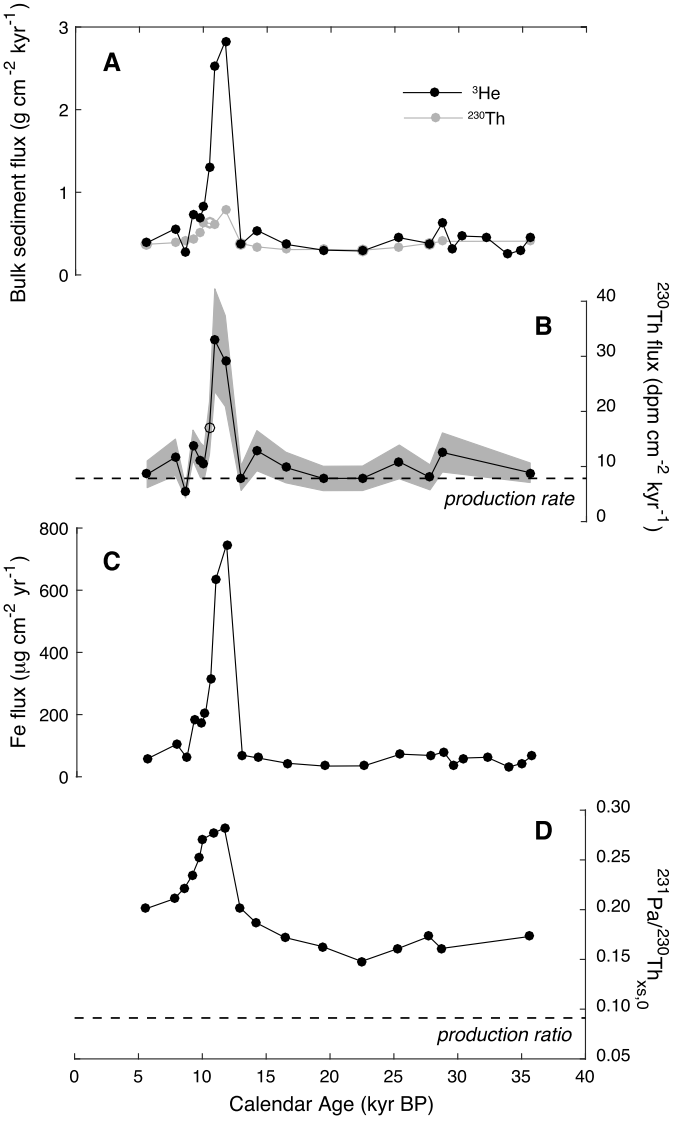

Fig. 3. ^{230}Th and ^{3}He results for core OC73-3-20. A) Bulk sediment flux estimated using ^{230}Th (grey circles) and ^{3}He (black circles), both in units of g cm^{-2} yr^{-1}, B) ^{230}Th flux (dpm cm^{-2} kyr^{-1}) estimated using ^{3}He compared to the ^{230}Th production rate for this water depth (dashed line), C) ^{3}He-normalized hydrothermal Fe flux (μg cm^{-2} yr^{-1}), and D) ^{231}Pa/^{230}Th activity ratio showing enhanced ^{231}Pa scavenging late in the deglaciation. The dashed line in panel D is the expected water column production ratio for Pa/Th. Note the ^{230}Th-normalized bulk sediment flux value at 10.47 kyr BP (open circle in panel A) is based on interpolation of two adjacent ^{230}Th$_{xs,0}$ results. The interpolated ^{230}Th$_{xs,0}$ value and measured ^{3}He concentration were used to determine the ^{230}Th flux at 10.47 kyr BP (open circle in panel B).

The ^{230}Th- and ^{3}He-normalized bulk sediment flux results for OC73-3-20 are shown in Fig. 3. The ^{3}He normalization technique is based on the accumulation of extra-terrestrial helium in the sediments (Farley et al., 2012). The two methods yield similar estimates from 35 to 15 kyr BP (~0.4 g cm^{-2} kyr^{-1}) but diverge abruptly at ~13 kyr BP, with ^{3}He-based fluxes peaking at 2.8 g cm^{-2} kyr^{-1} (Fig. 3a). By comparison, the ^{230}Th-based values peak at 0.6 g cm^{-2} kyr^{-1}. The difference between the two estimates decreases at ~10 kyr BP, with the ^{3}He-based values remaining 50% higher until 8 kyr BP, when the two methods once again yield consistent results of ~0.4 g cm^{-2} kyr^{-1}. Despite replicate ^{3}He measurements at each core depth, the ^{3}He-based fluxes are somewhat noisier than the ^{230}Th results, most likely due to the so-called 'nugget' effect, where statistical variations in the small number of interplanetary dust particles can yield variable extraterrestrial ^{3}He concentrations and therefore bulk sediment flux estimates (Farley et al., 2012).

The ^{3}He-normalized estimates of ^{230}Th flux for OC73-3-20 (Fig. 3b) and ^{231}Pa/^{230}Th ratios (Fig. 3d) show a similar pattern to the iron flux results. Prior to 14 kyr BP, ^{3}He-normalized ^{230}Th fluxes averaged 10 dpm cm^{-2} kyr^{-1}, elevated by ~25% relative to the water column production rate. The highest ^{230}Th fluxes (32 dpm cm^{-2} kyr^{-1}), which are approximately 4× higher than the water column production rate, coincide with the Fe flux maximum from 10 to ~13 kyr BP (Fig. 3c). The ^{231}Pa/^{230}Th results show

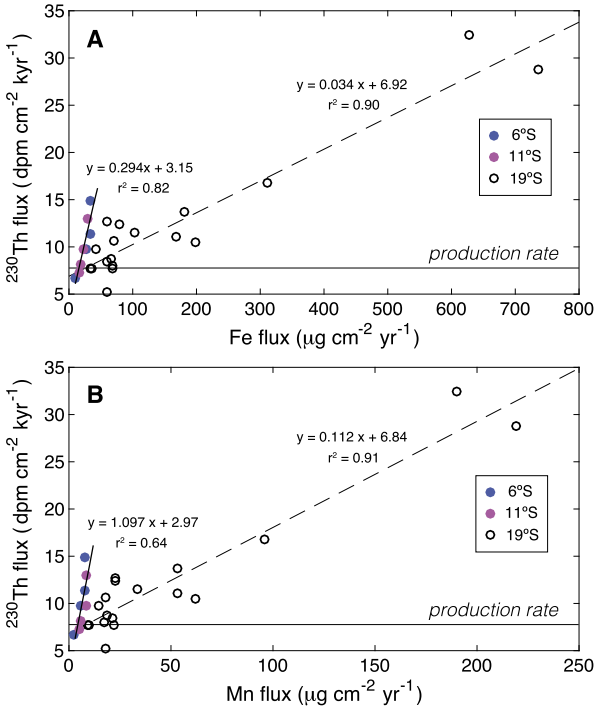

Fig. 4. Fe and Mn vs. ^{230}Th fluxes at 19°S (open circles), 11°S, and 6°S (filled circles). A) Fe flux vs. ^{230}Th flux. The intercept of the regression line for the 19°S results, where Fe fluxes equal zero, is 6.9 dpm cm^{-2} kyr^{-1}, similar to the ^{230}Th water column production rate (~7.9 dpm cm^{-2} kyr^{-1}). The slope of the regression line represents the nominal scavenging rate of ^{230}Th by Fe, equivalent to 34 dpm per g. For the 11°S and 6°S results, the intercept value is 3.1 dpm cm^{-2} kyr^{-1} and the ^{230}Th/Fe slope is 294 dpm per g. B) Mn flux vs. ^{230}Th flux. As in panel A, the intercept for the 19°S results (6.8 dpm cm^{-2} kyr^{-1}) is close to the water column production rate but the intercept for the 11°S and 6°S results is lower (3.0 dpm cm^{-2} kyr^{-1}). The ^{230}Th/Mn slope of the results from 11°S and 6°S is 1100 dpm per g, compared to 112 dpm/g at 19°S.

stable values throughout the LGM before increasing during the deglaciation (Fig. 3d). The highest ^{231}Pa/^{230}Th ratios (0.27–0.28) coincide with peak Fe fluxes from 10–13 kyr BP. The ^{231}Pa/^{230}Th ratios then decreased to 0.20 in the mid-Holocene, the same value observed prior to the deglacial peak.

We also measured ^{230}Th and ^{231}Pa during the LGM and deglaciation in cores Y71-07-49 at 11°S and Y71-09-106 at 6°S. The average ^{3}He-normalized ^{230}Th fluxes at the two sites is 10 dpm cm^{-2} kyr^{-1}, approximately 25% higher than the water column production rate (Fig. 4). Peak ^{230}Th fluxes, which coincide metal flux maxima at each site (Lund et al., 2016), are twice the water column production rate. The ^{231}Pa/^{230}Th activity ratios at 11°S and 6°S are also high, averaging 0.14, or ~50% greater than the production ratio (Table S8). Thus, enhanced scavenging of both ^{230}Th and ^{231}Pa occurred at 6°S, 11°S, and 19°S, sites that span ~1400 km of the SEPR.

3. Discussion

3.1. Hydrothermal scavenging of ^{230}Th

The strong linear correlation between Fe and ^{230}Th fluxes suggests that Fe-oxyhydroxides act as an important sink for ^{230}Th (Fig. 4a). The intercept of the regression for the 19°S results (where Fe fluxes equal zero) is 6.9 dpm cm^{-2} kyr^{-1}, close to the calculated water column production rate of ^{230}Th (7.9 dpm cm^{-2} kyr^{-1}). The slope of the regression, or the nominal scavenging rate of ^{230}Th per g of Fe, is 34 ± 3 dpm/g. Given that the bulk partition coefficient (K_d) for Mn-oxides is an order of magnitude larger than for Fe-oxyhydroxides (Hayes et al., 2015b), Mn-oxides may also play an important role in the scavenging of ^{230}Th. Similar to Fe, there is a strong correlation between Mn flux and ^{230}Th flux at 19°S (Fig. 4b). The slope of the regression is 19°S is 112 ± 9 dpm/g, or ~3× greater than that for iron. It is unclear whether this is due covariation between Fe and Mn (average Fe/Mn = 3.4) or preferential ^{230}Th scavenging by Mn.

At 6°S and 11°S, where peak deglacial Fe fluxes are 20–40 μg cm^{-2} yr^{-1}, ^{3}He-normalized ^{230}Th burial fluxes still exceed the water column production rate, even though the sites are >15 km from the ridge axis. For these locations, the ^{230}Th/Fe and ^{230}Th /Mn regression slopes are 293 ± 57 dpm/g and 1097 ± 340 dpm/g, respectively, or ~10× higher than their respective values at 19°S (Fig. 4). The greater sensitivity of ^{230}Th to hydrothermal particle flux at these sites may be due to variable entrainment of ambient water by hydrothermal plumes. A plume that rapidly forms large, sinking Fe particles before encountering a large volume of seawater would have lower Th/Fe ratios than a plume encountering greater volumes of seawater, and thus more ^{230}Th, before Fe particles settle to the seafloor. Entrainment is a function of vertical plume velocity, which in turn depends on heat flux and the density stratification of ambient seawater (Speer and Rona, 1989). Thus, more intense hydrothermal activity at 19°S may result in lower particulate ^{230}Th/metal ratios. Greater horizontal eddy diffusivities at low latitudes (Chiswell, 2013) may also facilitate transport of ^{230}Th towards the ridge axis at the sites closer to the equator.

Modern observations provide additional perspective on the scavenging efficiency of hydrothermal particles. At 15°S on the SEPR, the ^{230}Th/Fe ratio of suspended particles is 75 ± 18 dpm/g (Pavia et al., 2018), about twice the value observed in OC73-3-20. Further north on the EPR, plume particles corrected for sulfide inputs yield a ^{230}Th/Fe slope of 34 ± 14 dpm/g (German et al., 2002), similar to the slope for OC73-3-20. The ^{230}Th/Mn slope for the northern EPR data is much higher (803 ± 140) (German et al., 2002), but this is likely due to the proximity of the sediment traps to the hydrothermal plume (<200 m) and the long oxidation timescale for Mn^{2+} (Cowen et al., 1998). In the Atlantic, hydrothermal plume particles near the MAR have a ^{230}Th/Fe ratio of 78 ± 12 dpm/g (German et al., 1991; Lam et al., 2015; Hayes et al., 2015b). Given that the MAR particles have very high Fe/Mn ratios (Lam et al., 2015), these data imply that Fe-oxyhydroxides are the primary scavenging vector for ^{230}Th. Regardless of the exact cause, it is clear that hydrothermal scavenging drives the elevated ^{230}Th fluxes we observe at the SEPR core sites.

3.2. Implications for ^{230}Th normalization

Hydrothermal scavenging yields ^{230}Th fluxes higher than the water column production rate at all three sites (Fig. 4). In this situation the underlying premise of ^{230}Th-normalization, i.e. that ^{230}Th flux to the seafloor is only a function of ^{234}U decay in the overlying water column, no longer holds. While small deviations from the production rate have only a minor effect on bulk sediment fluxes, the ^{230}Th values reported here are up to 4× greater than expected from water column production. As a result, the implied bulk sediment fluxes at 19°S are spuriously low during the deglaciation (Fig. 3). Our results suggest that anomalous ^{230}Th scavenging at 19°S occurs when Fe fluxes are >50 μg cm^{-2} yr^{-1} (Fig. 4). At 6°S and 11°S, the threshold is closer to 25 μg cm^{-2} yr^{-1}. Sediment trap fluxes of ^{230}Th on the northern EPR display a similar sensitivity to scavenging by hydrothermally-derived iron (German et al., 2002).

Our results may have important implications for off-axis regions that supply ^{230}Th to the ridge crest, where lateral export of ^{230}Th will create deficits in dissolved ^{230}Th. If this phenomenon reduces ^{230}Th flux to the seafloor, it would yield artificially high bulk sediment fluxes. To estimate the magnitude of this effect during the

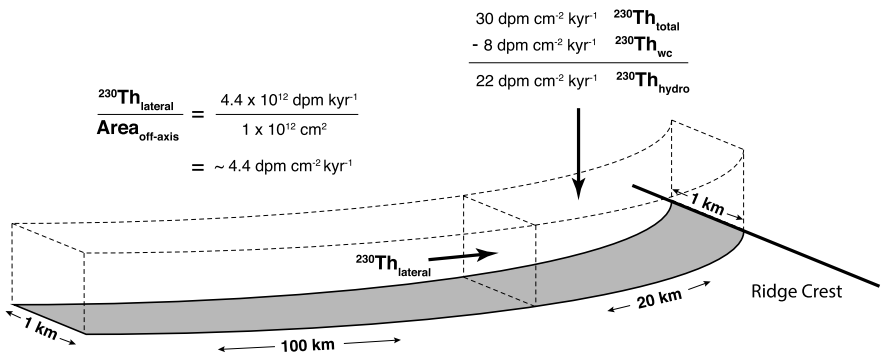

Fig. 5. Schematic depicting the influence of near-axis hydrothermal scavenging on off-axis ^{230}Th fluxes. Given nearly continuous plume coverage in this region of the SEPR today (Feely et al., 1996) and the likelihood of enhanced hydrothermal flux at multiple sites during the last deglaciation (Lund et al., 2016), we assume that the length scale of the hydrothermal sedimentation anomaly along axis is greater than the off-axis boxes depicted in the schematic. As such, the 1 km width of the box is meant to represent an arbitrary 1 km along-ridge section of the SEPR, while 20 km is the length-scale constrained by the three cores that show elevated ^{230}Th fluxes during the deglaciation (which range in distance from the ridge crest from 8 km to 28 km). Although this dimension is likely larger, we chose 20 km as a conservative estimate of the region over which elevated ^{230}Th scavenging likely occurs. Assuming a ^{230}Th flux of 30 dpm cm^{-2} kyr^{-1} within 20 km of the ridge axis, 8 dpm cm^{-2} kyr^{-1} of which is from water column production, the remainder is due to hydrothermal scavenging (22 dpm cm^{-2} kyr^{-1}). Over an area of 20 km^2, this equates to 4.4×10^{12} dpm kyr^{-1}. If the ^{230}Th originated from a 100 km × 1 km off-axis area, it would create an average deficit in this region of ~4.4 dpm cm^{-2} kyr^{-1}, approximately 50% of the water column production rate. If the off-axis area is larger (e.g. 1000 km), the associated ^{230}Th deficits are ~5% (Fig. S9).

deglaciation, we assume the average ^{230}Th flux from 0–20 km off-axis was 30 dpm cm^{-2} kyr^{-1} (Fig. 5). This value is constrained by peak ^{230}Th fluxes at 19°S (located 8 km from the ridge crest). The length scale is constrained by the results from 6°S, which demonstrate that elevated ^{230}Th fluxes occur up to 28 km off-axis. To simplify the calculations, we assume there was no hydrothermal scavenging >20 km off axis, which minimizes the axial ^{230}Th sink. If water column production accounts for 8 dpm cm^{-2} kyr^{-1} of the ^{230}Th flux near the ridge axis, the remainder can be attributed to hydrothermal scavenging (Fig. 5). Integrating 22 dpm cm^{-2} kyr^{-1} over 20 km^2 requires a lateral supply of 4.4×10^{12} dpm kyr^{-1}. If the ^{230}Th originated from up to 100 km off axis, it would create an average deficit in this region of 4.4 dpm cm^{-2} kyr^{-1}, or ~50% of the water column production rate, which would in turn would yield spuriously high ^{230}Th-normalized fluxes. If instead the ^{230}Th originated from up to 1000 km off axis, the deficit would be 5%, and the resulting impact would be minimal (Fig. S9). Note that our estimate of lateral ^{230}Th transport depends on the assumed ^{230}Th flux between the core site and ridge axis. If instead we use an average scavenging rate of 60 dpm cm^{-2} kyr^{-1}, the off-axis deficits increase by a factor of ~2 (Fig. S9).

Whether lateral transport of ^{230}Th can materially influence off axis sediment fluxes depends on two key factors, including the length scale of ^{230}Th diffusion and the along axis extent of hydrothermal scavenging. Assuming a ^{230}Th residence time (τ) of 10–30 yr (Hayes et al., 2015a) and a horizontal eddy diffusivity (K_h) of 300 m^2 s^{-1} in the region near 19°S (Chiswell, 2013; Katsumata and Yoshinari, 2010), we estimate the diffusive length scale for ^{230}Th (Δx) ranges from 400 to 700 km ($\Delta x = \sqrt{2K_H\tau}$) (Hayes et al., 2015a). On the short end of this range, on-axis scavenging may create significant off-axis deficits in dissolved ^{230}Th. At the longer end, scavenging would have only a minor impact. It is also important to note that our estimates assume the extent of hydrothermal plume coverage along the SEPR axis is equal to or greater than the diffusive length scale for ^{230}Th. If plumes act as spatially discrete sinks of ^{230}Th, then we would need to consider the radial area over which ^{230}Th is drawn toward a vent. In the case of the SEPR, however, approximately 60% of the ridge axis is overlain by hydrothermal plumes, with nearly continuous coverage from 17.5°S to 18.5°S (Beaulieu et al., 2013). Enhanced metal flux at multiple SEPR sites also implies that the overall plume coverage and extent was greater during the deglaciation (Lund et al., 2016). Given the uncertainties involved in determining the overall geochemical footprint of hydrothermal scavenging, there is a clear need for ^{3}He-normalized ^{230}Th fluxes from a grid of cores straddling the SEPR, from the ridge crest to 1000 km off axis.

Advection may also play a role in determining dissolved ^{230}Th distribution along the SEPR. Float trajectories suggest that near-axis flow from ~25°S to 15°S is predominantly to the north (Hautala and Riser, 1993). At 15°S, there is off-axis flow associated with the large westward flowing hydrothermal plume inferred from dissolved ^{3}He that reflects efflux of mantle-derived helium from the SEPR (Lupton and Jenkins, 2017). The dissolved ^{3}He data also reveal smaller scale plumes extending from ~23°S on the ridge axis towards the southwest and southeast (Lupton and Jenkins, 2017). Inverse modeling results reveal weak southwesterly flow on the western flank of the SEPR at 19°S (Faure and Speer, 2012), consistent with the ^{3}He tracer field. Inferred flow on the eastern flank is more complex; high dissolved ^{3}He values that trend southeast from ~23°S may be associated with counter-clockwise circulation and plume transport from further south on the SEPR (Faure and Speer, 2012). Float trajectories near the core sites at 11°S and 6°S imply the mean flow is to the north and west, similar to the pattern at 19°S (Hautala and Riser, 1993).

If advection plays a role in controlling dissolved ^{230}Th near the SEPR, then deep water flowing from 19°S to 6°S should become progressively depleted in ^{230}Th due to hydrothermal scavenging along axis (Pavia et al., 2019). This would in turn increase the lateral off-axis concentration gradient, thereby promoting the diffusive flux of ^{230}Th towards the ridge axis. This may in part explain why the 11°S and 6°S sites to have greater ^{230}Th flux per unit iron flux to the sediments (Fig. 4). Regardless of whether advection is predominantly northward or southward at the core sites, topographically-steered flow of plumes should yield a persistent rain of metalliferous particles parallel to the ridge axis (Speer et al., 2003). We anticipate the resulting hydrothermal scavenging would create dissolved ^{230}Th deficits along axis that would promote diffusion of ^{230}Th from the flanks of the SEPR.

3.3. Scavenging of additional metals

The ^{231}Pa/^{230}Th results for OC73-3-20 provide additional insight into the scavenging history on the SEPR. Like ^{230}Th, the scavenging residence time of ^{231}Pa is short relative to its radioactive half-life (Henderson and Anderson, 2003). Given that the production rate of both ^{231}Pa and ^{230}Th is predictable, so too is their activity ratio (~0.093). Deviations from the production ratio in sediments is due to variations in particle composition and greater

lateral transport of ^{231}Pa, which has a scavenging residence time of centuries compared to decades for ^{230}Th (Henderson and Anderson, 2003). Dissolved ^{231}Pa is particularly susceptible to scavenging by metalliferous particles; near-axis particulate ^{231}Pa/^{230}Th ratios at 15°S on the SEPR average 0.15, well above the production ratio (Pavia et al., 2018). In core OC73-3-20, ^{231}Pa/^{230}Th averaged 0.20 over the past 40 kyr (Fig. 3c). The ratio peaked at 0.28 late in deglaciation, corresponding to the interval of elevated Fe flux (Fig. 3d). In cores Y71-07-49 and Y71-09-106, all of ^{231}Pa/^{230}Th results are above the production ratio, with peak values (0.14) occurring during the deglaciation (Table S8). The ^{231}Pa/^{230}Th results are therefore consistent with anomalous hydrothermal scavenging. At 19°S, decreasing ^{231}Pa/^{230}Th from 10 to 5 kyr BP tracks the shift in Fe flux, suggesting that declining plume output resulted in reduced scavenging of ^{231}Pa relative to ^{230}Th from bottom waters. The ^{231}Pa/^{230}Th ratios and Fe fluxes for OC73-3-20 are anomalously high relative to results from other locations in the Pacific, suggesting that this site is an endmember scavenging case (Fig. S7).

Our results suggest that hydrothermal scavenging is an important contributor to basin-scale ^{231}Pa water column removal throughout the last 40 kyr—an effect that is most pronounced from 5–15 kyr BP, when ^{231}Pa/^{230}Th ratios were 2–3× higher than the production ratio (Fig. 3). Because ^{231}Pa is more slowly scavenged by particles falling through the water column than ^{230}Th, it is more susceptible to boundary scavenging (Hayes et al., 2015b). As a result, the ^{231}Pa/^{230}Th ratio for hydrothermal precipitates is typically higher than for other open ocean particles (Pavia et al., 2018). Elevated ^{231}Pa/^{230}Th ratios imply that hydrothermal fallout stripped dissolved ^{231}Pa from the water column, therefore creating a lateral gradient that facilitated ^{231}Pa diffusion towards the ridge crest. Core top ^{231}Pa/^{230}Th ratios in the central Pacific are typically lower than the production ratio, balanced by higher values in the Subarctic, eastern equatorial Pacific, and the Southern Ocean, a spatial distribution that has been attributed to boundary scavenging (Hayes et al., 2014). Our results support the idea that metalliferous sediments act as a boundary sink for ^{231}Pa.

Hydrothermal scavenging also played a key role in controlling the fluxes of V, As, Zn, and Cu at 19°S. The fluxes of these metals increased ∼12× late in the deglaciation, likely due to scavenging by or co-precipitation with Fe-oxyhydroxides (Fig. S6). Results from 1°N, 6°S and 11°S show similar but more modest changes (3–5×) during T1 (Frank et al., 1994; Lund et al., 2016). These results suggest that deglacial scavenging rates on the SEPR were at least 3× higher than today, with potentially important implications for the budget of oxyanions. For example, hydrothermal removal accounts for approximately 50% of the oceanic sink for V, which has a residence time of ∼100 kyr (Schlesinger et al., 2017). If V removal along the global mid-ocean ridge system varies on glacial–interglacial timescales, then the underlying assumption of steady state conditions for the oceanic V budget would need to be revisited.

3.4. Implications for other ridges

We anticipate that scavenging behavior at other mid-ocean ridges was similar to the SEPR. Multiple ridges experienced elevated hydrothermal activity during the deglaciation, which likely caused anomalous ^{230}Th scavenging and lateral transport of ^{230}Th toward ridge axes (Lalou et al., 1998; Lund et al., 2016; Middleton et al., 2016; Costa et al., 2017) (Fig. 6). The overall spatial extent of off-axis ^{230}Th deficits is difficult to constrain *a priori* given: 1) uncertainty in the length scale of ^{230}Th diffusion, 2) intra- and inter-ridge differences in hydrothermal output, and 3) the magnitude of the deglacial metal flux signal. Instead, we suggest that bulk sediment fluxes for cores collected within a few hundred kilometers of ridge axes be constrained using both ^{230}Th and ^{3}He to address the potential influence of hydrothermal scavenging. More broadly, our results support the idea that mid-ocean ridges are important boundary scavenging locations for trace metals in the deep ocean (German et al., 2002). Given that reconstructions thus far indicate that the Holocene was an interval of relatively low hydrothermal output (Costa et al., 2017; Middleton et al., 2016; Lund et al., 2016; Lalou et al., 1998), scavenging rates based on modern fluxes will tend to underestimate the role of hydrothermal scavenging in trace metal removal from the deep ocean.

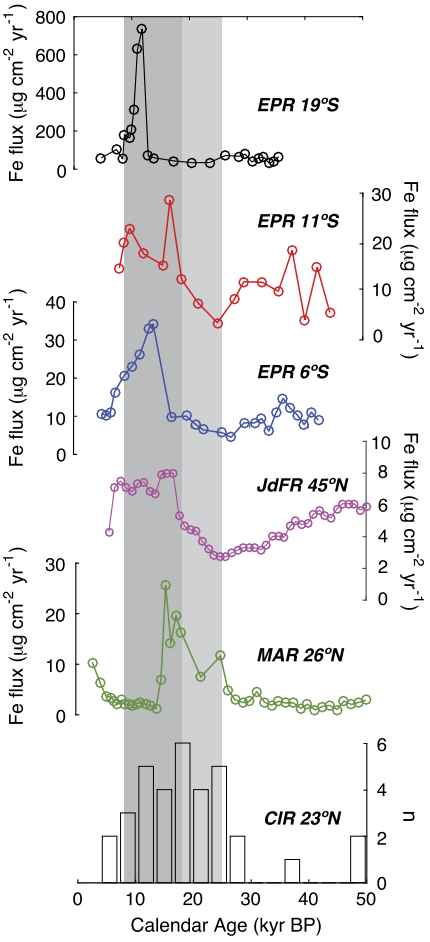

Fig. 6. Reconstructions of hydrothermal activity at six locations, including the EPR at 19°S (this study), 11°S (Lund et al., 2016), and 6°S (Lund et al., 2016), the JdFR at 45°N (Costa et al., 2017), the MAR at 26°N (Middleton et al., 2016), and the CIR at 23°N (Lalou et al., 1998). The EPR and MAR results are ^{3}He-normalized fluxes, while the JdFR results are based on ^{230}Th-normalization. The CIR results are presented as a histogram of U/Th dated relict sulfide chimneys and mounds. Also shown are the time intervals for the LGM (19–26 kyr BP; light grey vertical bar) and deglaciation (8–18 kyr BP; darker grey vertical bar) based on sea level and ice sheet reconstructions (Fleming et al., 1998; Clark et al., 2009).

3.5. Drivers of the Fe and Mn flux anomalies

In addition to hydrothermal activity, several factors can influence metal fluxes to ridge flank sediments, including variations in sediment focusing, diagenetic remobilization, and the oxidation rate of reduced Fe emanating from vents. Sediment focusing is an implausible explanation of our results given the similar pattern at multiple EPR locations. ^{3}He-based estimates of focusing factors at 6°S and 11°S are also inconsistent with lateral focusing of hydrothermal particles (Lund et al., 2016). Diagenetic remobilization of metals after deposition is an equally unlikely ex-

planation of the SEPR results for several reasons. First, organic carbon (C_{org}) levels at 19°S are too low to remobilize the quantity of Fe observed during Termination 1 (T1). Fe concentrations reach 25% by weight from 8 to 12 kyr BP (Fig. S4). If the required C_{org} originated from this interval, the quantity necessary for reducing Fe would be approximately 1.3% (Froelich et al., 1979), or 3–4 times the C_{org} estimates for this interval (Fig. S2). A similar pattern occurs at 11°S, where organic carbon levels of 0.1–0.2% are too low to mobilize the quantity of Fe observed (Lund et al., 2016). Second, diagenetic remobilization would likely create metal peaks that are offset in depth within each core (Froelich et al., 1979), yet the Fe and Mn at 19°S are synchronous, similar to the pattern at 6°S and 11°S (Fig. 2). Third, the mean down core Fe/Mn ratio at 19°S (3.4 ± 0.4) is similar to the inferred hydrothermal endmember for the SEPR (3.45) (Dymond, 1981; Dunk and Mills, 2006). Taken together, these results imply that hydrothermal sedimentation was the primary driver of the signal at 19°S.

Given that the SEPR data are incompatible with sediment focusing and diagenetic overprinting, the flux maxima must be related to either hydrothermal output or changes in Fe oxidation rate. As deep water flows from the Atlantic to the Pacific, respiration of organic matter drives the consumption of oxygen, the accumulation of dissolved inorganic carbon, and hence a decrease in pH. As a result, the oxidation rate half-life of Fe^{2+} is slower at the EPR (~3 h) than the MAR (~30 min) (Field and Sherrell, 2000). Cullen and Coogan (2017) suggest that enhanced ventilation of the deep Pacific during glacial terminations resulted in higher pH and oxygen levels, which in turn caused enhanced fallout of Fe-rich hydrothermal particles near ridge axes.

Several features of the SEPR records are inconsistent with the oxidation rate hypothesis. Hydrothermal Fe^{2+} is oxidized in minutes to hours while Mn^{2+} is oxidized in weeks to months (Cowen et al., 1998). The contrasting timescales allow Mn^{2+} to be used as conservative tracer of vent fluid dilution as Fe^{2+} is oxidized (Field and Sherrell, 2000). It is therefore highly unlikely that variations in deep Pacific oxygen and pH levels would drive synchronous changes in Fe and Mn flux to ridge flank sediments. Cullen and Coogan (2017) speculate that global deposition of Mn from bottom waters could account for coherent Fe and Mn signals, but such a mechanism cannot explain the factor of three difference in Mn flux to the eastern and western flanks of the SEPR during Terminations 1 and 2 (Lund et al., 2016) or the much larger Mn fluxes at 19°S (Fig. 2). The relative timing of SEPR signals is also inconsistent with the oxidation rate hypothesis; at 19°S, the flux of Fe began to increase at ~13 kyr BP, approximately 3–5 kyr later than at 6°S and 11°S. If the signals were driven by variable deep Pacific pH and oxygen levels, they should align within age model uncertainty.

The oxidation rate mechanism is also unable to account for hydrothermal reconstructions from the Mid-Atlantic Ridge (MAR) and Central Indian Ridge (CIR). On the MAR, iron fluxes increased early in the deglaciation (Middleton et al., 2016), similar to the pattern at 6°S and 11°S on the SEPR (Fig. 6). Given that ventilation of the deep Atlantic slowed during Heinrich Stadial 1 (14.5–17.5 kyr BP) (McManus et al., 2004), the residence time of deep water would have increased, resulting in generally lower pH and oxygen levels (Schmittner and Lund, 2015). This would in turn yield slower Fe^{2+} oxidation rates, which should minimize iron fluxes to ridge flank sediments, opposite the observed pattern. U/Th-dated relict sulfide chimneys and mounds from the CIR also show a peak in sample frequency from 10 to 25 kyr BP (Fig. 6) (Lalou et al., 1998). Given that the formation of sulfide deposits should occur independently of ambient deep ocean conditions, these data imply there was enhanced hydrothermal output on the CIR during the LGM and deglaciation. Variations in hydrothermal activity, rather than deep ocean oxidation rates, is therefore the simplest explanation of the results from the Atlantic, Pacific, and Indian basins.

The timing offset between hydrothermal flux maxima on the SEPR and between the SEPR and other ridges is most likely due to geological factors. If the records reflect glacially-driven variations in magmatic flux to ridge axes, the signal should lag sea level forcing by thousands of years due to slow melt extraction velocities in the upper mantle (Lund and Asimow, 2011). However, these velocities are uncertain and it is unclear how they vary from one ridge segment to another. Besides obvious sources of difference like the depth of the major melting regime, which is thought to depend primarily on mantle potential temperature (Klein and Langmuir, 1987), there are asymmetrically spreading ridges where the most productive part of the melting regime is shifted horizontally from the axis (Forsyth et al., 1998). Additionally, all theories of melt migration presently have free parameters such as a reference permeability that allow for considerable variation in the arrival time of melt at the ridge axis. In general, therefore, the theory that hydrothermal output reflects modulation of melt production by sea level naturally predicts that different ridge segments will display flux peaks at somewhat different times after a major sea level fall, but we do not yet have a theoretical understanding of which segments should peak earlier or later. In fact, as we have argued previously (Lund et al., 2016) the timing of sea level-modulated magmatic variations on ridge segments may provide the best available tool with which to refine our highly uncertain models of melt migration at mid-ocean ridges, including using variations in the lag time to identify which segment-scale parameters promote faster or slower melt migration.

4. Conclusions

Hydrothermal plume particles are highly efficient at scavenging dissolved ^{230}Th and ^{231}Pa from the deep ocean. While this effect has long been known to occur near mid-ocean ridges (German et al., 1991, 2002), results from the GEOTRACES program show that the spatial imprint of hydrothermal scavenging is larger than previously assumed (Hayes et al., 2015a; Pavia et al., 2018). Emerging evidence from multiple ridges also suggests that hydrothermal activity varies on glacial–interglacial timescales, with peak metal fluxes occurring during terminations (Lund et al., 2016; Middleton et al., 2016; Costa et al., 2017). Together, these observations suggest that scavenging of trace metals should be most pronounced during glacial terminations, with potentially important implications for oceanic trace metal budgets and the use of ^{230}Th as a constant flux proxy.

Here we evaluate hydrothermal fluxes and trace metal scavenging using a core from 19°S on the super-fast section of the SEPR, one of the most hydrothermally active ridges on Earth. The fluxes of Fe, Mn, Cu, Zn, As, and V peak late in the deglaciation, reaching ~12× higher than background levels. The maxima in Fe and Mn flux are an order of magnitude greater than other SEPR locations and higher than any ridge crest metal fluxes in the published literature. Low sedimentary organic carbon concentrations preclude the possibility that the Fe and Mn signals are a byproduct of diagenesis. Our results are also inconsistent with metal deposition driven by variable bottom water redox conditions because Fe fluxes at 19°S lag those at 6°S and 11°S by several thousand years and the downcore Fe/Mn ratio at 19°S is in excellent agreement with the hydrothermal endmember Fe/Mn ratio for this region. Instead, the simplest explanation of the 19°S results is enhanced hydrothermal activity.

We estimate the flux of ^{230}Th to ridge flank sediments using ^{3}He-normalized bulk sediment accumulation rates. Overall, the reconstructed ^{230}Th fluxes are similar to the water column pro-

duction rate, with the exception of 8–13 kyr BP, when Fe and Mn accumulation rates were anomalously high. In this interval, ^{230}Th fluxes are up to 4× greater than predicted by water column production. ^{231}Pa/^{230}Th ratios are higher than the production ratio throughout the record and peak from 8–13 kyr BP, which is consistent with the preferential scavenging of ^{231}Pa by hydrothermal particles (Hayes et al., 2015a; Pavia et al., 2018). We report similar results for sites at 6°S and 11°S on the SEPR. The data therefore suggest that the SEPR acts as a boundary scavenging location in the open ocean. The effect varies on glacial–interglacial timescales and was the most pronounced during the last deglaciation.

The combination of ^{3}He, ^{230}Th, and Fe analyses in several SEPR cores allows us to assess the threshold above which hydrothermal particle fallout causes anomalous ^{230}Th scavenging. Our results suggest that ^{230}Th fluxes exceed the water column production rate when Fe fluxes are greater than ∼25 $\mu g\,cm^{-2}\,yr^{-1}$. The surplus in sedimentary ^{230}Th yields bulk fluxes derived by traditional ^{230}Th-normalization that are spuriously low; we find that ^{230}Th-based bulk sediment mass fluxes are up to 4× lower than those estimated using ^{3}He. Lateral diffusion of ^{230}Th towards the ridge axis may produce off-axis deficits in dissolved ^{230}Th, which would in turn decrease ^{230}Th flux to ridge flank sediments and yield artificially high ^{230}Th-normalized accumulation rates. On the SEPR, we estimate this could bias bulk sediment fluxes by 5–50%, depending on the length scale of ^{230}Th diffusion and the along axis extent of hydrothermal scavenging. A full quantification of the effect will require estimates of ^{230}Th flux from a cross-axis transect of sediment cores. High-resolution water column sampling is also necessary to map spatial gradient is dissolved ^{230}Th. In the interim, we suggest that hydrothermal fluxes in ridge settings be constrained using both ^{3}He and ^{230}Th.

If changes in ^{230}Th burial create biased estimates of sedimentary mass flux in ridge flank settings, the fluxes of many constituents (e.g. opal, $CaCO_3$, productivity proxies, dust, etc.) would be expected to co-vary. Additionally, temporal changes in these variables can be compared to nearby records that are further off axis to assess for anomalous scavenging effects. For example, if a deglacial peak in dust flux were identified in a core on the EPR ridge flank, this would be at odds with previous dust records showing peak dust fluxes during glacial periods from locations spanning the latitudinal range of the Pacific (Anderson et al., 2006).

In combination with published EPR records from 1°N, 6°S, and 11°S, the results presented here suggest the last deglaciation was broadly characterized by enhanced hydrothermal sedimentation from the equator to 19°S, a distance of ∼2200 km. Hydrothermal records from the Mid-Atlantic Ridge, Central Indian Ridge, and Juan de Fuca Ridge also show maxima from ∼10 to 20 kyr BP. Given opposing circulation changes in the Atlantic and Pacific during the last deglaciation, it is highly unlikely that variations in deep ocean pH and oxygen were the primary driver of the hydrothermal time series. We instead suggest the most likely cause is enhanced hydrothermal activity mediated by glacial–interglacial changes in sea level. Given the correspondence between magmatic budget and hydrothermal plume incidence today (Baker and German, 2004), the hydrothermal reconstructions suggest that magmatic activity increased as sea level was rising, which at face value appears to contradict the sea level hypothesis. However, the magmatic expression of sea level variability at mid-ocean ridges should lag the initial forcing by thousands of years due to the slow rate of melt migration in the upper mantle (Lund and Asimow, 2011). Thus, enhanced hydrothermal activity during the last deglaciation may reflect falling sea level during intervals of ice sheet growth, such as the Last Glacial Maximum or Marine Isotope Stage 4.

Acknowledgements

DCL, EIS, and SM were supported by NSF award OCE-1558641 and the UCONN Research Excellence Program. We are grateful to David Cady at UCONN for assistance with ICP-MS analyses, Jean Lynch-Stieglitz at Georgia Tech for assistance with stable isotope analyses, and Martin Fleisher at LDEO for assistance with ^{230}Th and ^{231}Pa analyses. We are also indebted to the Oregon State University Core Repository for the curation of core OC73-3-20. The OSU Repository is supported by NSF award OCE-1558679. PDA was supported by NSF awards OCE-1558372 and EAR-1551433. FJP was supported by an NSF-GRFP (DGE-16-44869). All data needed to evaluate the conclusions in the paper are present in the paper and/or the Supplementary Materials.

Appendix A. Supplementary material

Supplementary material related to this article can be found online at https://doi.org/10.1016/j.epsl.2018.12.037.

References

Albani, S., Mahowald, N.M., Winckler, G., Anderson, R.F., Bradtmiller, L.I., Delmonte, B., 2015. Twelve thousand years of dust: the Holocene global dust cycle constrained by natural archives. Clim. Past 11 (6), 869–903.
Anderson, R.F., Bacon, M.P., Brewer, P.G., 1983. Removal of ^{230}Th and ^{231}Pa from the open ocean. Earth Planet. Sci. Lett. 62 (1), 7–23.
Anderson, R.F., Ali, S., Bradtmiller, L.I., Nielsen, S.H.H., Fleisher, M.Q., Anderson, B.E., 2009. Wind-driven upwelling in the Southern Ocean and the deglacial rise in atmospheric CO_2. Science 323 (5920), 1443–1448.
Anderson, R., Fleisher, M., Lao, Y., 2006. Glacial–interglacial variability in the delivery of dust to the central equatorial Pacific Ocean. Earth Planet. Sci. Lett. 242 (3–4), 406–414.
Bacon, M.P., Anderson, R.F., 1982. Distribution of thorium isotopes between dissolved and particulate forms in the deep sea. J. Geophys. Res., Oceans 87, 2045–2056.
Bacon, M.P., 1988. Tracers of chemical scavenging in the ocean: boundary effects and large-scale chemical fractionation. Philos. Trans. R. Soc. Lond., Ser. A 325, 147–160.
Baker, E.T., German, G.R., 2004. On the global distribution of hydrothermal vent fluids. In: Mid-Ocean Ridges: Hydrothermal Interactions Between the Lithosphere and Oceans. American Geophysical Union, pp. 245–266.
Beaulieu, S.E., Baker, E.T., German, C.R., Maffei, A., 2013. An authoritative global database for active submarine hydrothermal vent fields. Geochem. Geophys. Geosyst. 14 (11), 4892–4905.
Bruland, K.W., Lohan, M.C., 2003. Controls of trace metals in seawater. In: Treatise on Geochemistry, vol. 6, pp. 23–47.
Chiswell, S.M., 2013. Lagrangian time scales and eddy diffusivity at 1000 m compared to the surface in the South Pacific and Indian Oceans. J. Phys. Oceanogr. 43 (12), 2718–2732.
Clark, P.U., Dyke, A.S., Shakun, J.D., Carlson, A.E., Clark, J., Wohlfarth, B., et al., 2009. The Last Glacial Maximum. Science 325 (5941), 710–714.
Costa, K.M., McManus, J.F., Middleton, J.L., Langmuir, C.H., Huybers, P.J., Winckler, G., et al., 2017. Hydrothermal deposition on the Juan de Fuca ridge over multiple glacial–interglacial cycles. Earth Planet. Sci. Lett. 479, 120–132.
Cowen, J.P., Bertram, M.A., Baker, E.T., Feely, R.A., Massoth, G.J., Summit, M., 1998. Geomicrobial transformation of manganese in Gorda Ridge event plumes. Deep-Sea Res., Part 2, Top. Stud. Oceanogr. 45 (12), 2713–2737.
Cullen, J.T., Coogan, L.A., 2017. Changes in Fe oxidation rate in hydrothermal plumes as a potential driver of enhanced hydrothermal input to near-ridge sediments during glacial terminations. Geophys. Res. Lett. 44 (23), 11,951–11,958.
Dunk, R.M., Mills, R.A., 2006. The impact of oxic alteration on plume-derived transition metals in ridge flank sediments from the east pacific rise. Mar. Geol. 229 (3–4), 133–157.
Dymond, J., 1981. Geochemistry of Nazca Plate surface sediments – an evaluation of hydrothermal, biogenic, detrital, and hydrogenous sources. In: Geological Society of America Memoirs, vol. 154, pp. 133–173.
Dymond, J., Roth, S., 1988. Plume dispersed hydrothermal particles: a time-series record of settling flux from the Endeavour Ridge using moored sensors. Geochim. Cosmochim. Acta 52, 2525–2536.
Farley, K.A., Montanari, A., Coccioni, R., 2012. A record of the extraterrestrial ^{3}He flux through the late cretaceous. Geochim. Cosmochim. Acta 84, 314–328.
Faure, V., Speer, K., 2012. Deep circulation in the eastern South Pacific Ocean. J. Mar. Res. 70, 748–778.
Field, M.P., Sherrell, R.M., 2000. Dissolved and particulate Fe in a hydrothermal plume at 9°45′N, East Pacific Rise: slow Fe (II) oxidation kinetics in Pacific plumes. Geochim. Cosmochim. Acta 64 (4), 619–628.

Fleming, K., Johnston, P., Zwartz, D., Yokoyama, Y., Lambeck, K., Chappell, J., 1998. Refining the eustatic sea-level curve since the last glacial maximum using far- and intermediate-field sites. Earth Planet. Sci. Lett. 163 (1–4), 327–342.

Forsyth, D.W., Scheirer, D.S., Webb, S.C., Dorman, L.M., Orcutt, J.A., Harding, A.J., 1998. Imaging the deep seismic structure beneath a mid-ocean ridge: the MELT experiment. Science 280 (5367), 1215–1218.

Francois, R., Frank, M., van der Loeff, M.M.R., Bacon, M.P., 2004. ^{230}Th normalization: an essential tool for interpreting sedimentary fluxes during the late quaternary. Paleoceanography 19 (1), 16.

Frank, M., Eckhardt, J.D., Eisenhauer, A., Kubik, P.W., Dittrichhannen, B., Segl, M., et al., 1994. Beryllium 10, Thorium 230, and Protoactinium 231 in Galapagos microplate sediments – implications of hydrothermal activity and paleoproductivity changes during the last 100,000 years. Paleoceanography 9 (4), 559–578.

Feely, R.A., Baker, E.T., Marumo, K., Urabe, T., Ishibashi, J., Gendron, J., Lebon, G.T., Okamura, K., 1996. Hydrothermal plume particles and dissolved phosphate over the superfast-spreading southern East Pacific Rise. Geochim. Cosmochim. Acta 60, 2297–2323.

Froelich, P.N., Klinkhammer, G.P., Bender, M.L., Luedtke, N.A., Heath, G.R., Cullen, D., et al., 1979. Early oxidation of organic-matter in pelagic sediments of the eastern equatorial Atlantic – suboxic diagenesis. Geochim. Cosmochim. Acta 43 (7), 1075–1090.

German, C.R., Fleer, A.P., Bacon, M.P., Edmond, J.M., 1991. Hydrothermal scavenging at the Mid-Atlantic Ridge: radionuclide distributions. Earth Planet. Sci. Lett. 105 (1–3), 170–181.

German, C.R., Seyfried, W.E., 2014. Hydrothermal processes. In: Mottl, M.J., Elderfield, H. (Eds.), Treatise on Geochemistry, vol. 8, pp. 191–223.

German, C.R., Colley, S., Palmer, M.R., Khripounoff, A., Klinkhammer, G.P., 2002. Hydrothermal plume-particle fluxes at 13°N on the East Pacific Rise. Deep-Sea Res., Part 1, Oceanogr. Res. Pap. 49 (11), 1921–1940.

Hayes, C.T., Anderson, R.F., Fleisher, M.Q., Serno, S., Winckler, G., Gersonde, R., 2014. Biogeography in ^{231}Pa/^{230}Th ratios and a balanced ^{231}Pa budget for the Pacific Ocean. Earth Planet. Sci. Lett. 391, 307–318.

Hayes, C.T., Anderson, R.F., Fleisher, M.Q., Huang, K., Robinson, L.F., Lu, Y., 2015a. ^{230}Th and ^{231}Pa on GEOTRACES GA03, the U.S. GEOTRACES North Atlantic transect, and implications for modern and paleoceanographic chemical fluxes. Deep-Sea Res., Part 2, Top. Stud. Oceanogr. 116, 29–41.

Hayes, C.T., Anderson, R.F., Fleisher, M.Q., Vivancos, S.M., Lam, P.J., Ohnemus, D.C., 2015b. Intensity of Th and Pa scavenging partitioned by particle chemistry in the North Atlantic Ocean. Mar. Chem. 170, 49–60.

Hautala, S.L., Riser, S.C., 1993. A nonconservative beta-spiral determination of the deep circulation in the eastern south Pacific. J. Phys. Oceanogr. 23, 1975–2000.

Henderson, G.M., Heinze, C., Anderson, R.F., Winguth, A.M.E., 1999. Global distribution of the ^{230}Th flux to ocean sediments constrained by GCM modelling. Deep-Sea Res., Part 1, Oceanogr. Res. Pap. 46 (11), 1861–1893.

Henderson, G.M., Anderson, R.F., 2003. The U-series toolbox for paleoceanography. Rev. Mineral. Geochem. 52 (1), 493–531.

Katsumata, K., Yoshinari, H., 2010. Uncertainties in global mapping of ARGO drift data at the parking level. J. Oceanogr. 66 (4), 553–569.

Khripounoff, A., Alberic, P., 1991. Settling of particles in a hydrothermal vent field (East Pacific Rise 13°N) measured with sediment traps. Deep-Sea Res., Part 1, Oceanogr. Res. Pap. 38, 729–744.

Kienast, S.S., Kienast, M., Mix, A.C., Calvert, S.E., Francois, R., 2007. Thorium-230 normalized particle flux and sediment focusing in the Panama Basin region during the last 30,000 years. Paleoceanography 22 (2), 19.

Klein, E.M., Langmuir, C.H., 1987. Global correlations of ocean ridge basalt chemistry with axial depth and crustal thickness. J. Geophys. Res. 92 (B8), 8089–8115.

Lalou, C., Munch, U., Halbach, P., Reyss, J.L., 1998. Radiochronological investigation of hydrothermal deposits from the MESO zone, Central Indian Ridge. Mar. Geol. 149 (1–4), 243–254.

Lam, P.J., Ohnemus, D.C., Auro, M.E., 2015. Size-fractionated major particle composition and concentrations from the US GEOTRACES North Atlantic zonal transect. Deep-Sea Res., Part 2, Top. Stud. Oceanogr. 116, 303–320.

Lilley, M.D., Feely, R.A., Trefry, J.H., 1995. Chemical and biochemical transformations in hydrothermal plumes. In: Hydrothermal Systems: Physical, Chemical, Biological, and Geological Interactions. In: Geophysical Monograph, vol. 91. American Geophysical Union.

Lopez, G.I., Marcantonio, F., Lyle, M., Lynch-Stieglitz, J., 2015. Dissolved and particulate ^{230}Th–^{232}Th in the central equatorial Pacific Ocean: evidence for far-field transport of the east pacific rise hydrothermal plume. Earth Planet. Sci. Lett. 431, 87–95.

Lund, D.C., Asimow, P.D., 2011. Does sea level influence mid-ocean ridge magmatism on Milankovitch timescales? Geochem. Geophys. Geosyst. 12, 26.

Lund, D.C., Asimow, P.D., Farley, K.A., Rooney, T.O., Seeley, E., Jackson, E.W., 2016. Enhanced East Pacific Rise hydrothermal activity during the last two glacial terminations. Science 351 (6272), 478–482.

Lund, D.C., Seeley, E.I., Asimow, P.D., Lewis, M., McCart, S., Mudahy, A., 2018. Anomalous Pacific-Antarctic Ridge volcanism precedes glacial Termination 2. Geochem. Geophys. Geosyst. 19, 2478–2491.

Lupton, J.E., Jenkins, W.J., 2017. Evolution of the south Pacific helium plume over the past three decades. Geochem. Geophys. Geosyst. 18, 1810–1823.

Marchig, V., Erzinger, J., Heinze, P.M., 1986. Sediments in the black smoker area of the East Pacific Rise (18.5°S). Earth Planet. Sci. Lett. 79, 93–106.

Martínez, C.E., McBride, M.B., 1998. Coprecipitates of Cd, Cu, Pb and Zn in iron oxides: solid phase transformation and metal solubility after aging and thermal treatment. Clays Clay Miner. 46 (5), 537–545.

McGee, D., Winckler, G., Borunda, A., Serno, S., Anderson, R.F., Recasens, C., et al., 2016. Tracking eolian dust with helium and thorium: impacts of grain size and provenance. Geochim. Cosmochim. Acta 175, 47–67. https://doi.org/10.1016/j.gca.2015.11.023.

McManus, J.F., Francois, R., Gherardi, J.M., Keigwin, L.D., BrownLeger, S., 2004. Collapse and rapid resumption of Atlantic meridional circulation linked to deglacial climate changes. Nature 428 (6985), 834–837.

Middleton, J.L., Langmuir, C.H., Mukhopadhyay, S., McManus, J.F., Mitrovica, J.X., 2016. Hydrothermal iron flux variability following rapid sea level changes. Geophys. Res. Lett. 43 (8), 3848–3856.

Pavia, F., Anderson, R., Vivancos, S., Fleisher, M., Lam, P., Lu, Y., et al., 2018. Intense hydrothermal scavenging of ^{230}Th and ^{231}Pa in the deep Southeast Pacific. Mar. Chem. 201, 212–228. https://doi.org/10.1016/j.marchem.2017.08.003.

Pavia, F., et al., 2019. Timescales of hydrothermal scavenging in the South Pacific Ocean from ^{234}U, ^{230}Th, and ^{232}Th. Earth Planet. Sci. Lett. 506, 146–156.

Resing, J.A., Sedwick, P.N., German, C.R., Jenkins, W.J., Moffett, J.W., Sohst, B.M., et al., 2015. Basin-scale transport of hydrothermal dissolved metals across the south Pacific Ocean. Nature 523 (7559), 200–203.

Ryan, W.B.F., Carbotte, S.M., Coplan, J.O., O'Hara, S., Melkonian, A., Arko, R., et al., 2009. Global multi-resolution topography synthesis. Geochem. Geophys. Geosyst. 10, 9.

Rudnicki, M.D., Elderfield, H., 1993. A chemical model of the buoyant and neutrally buoyant plume above the TAG vent field, 26 degrees N, Mid-Atlantic Ridge. Geochim. Cosmochim. Acta 57, 2939–2957.

Savenko, A.V., 2001. Co-precipitation of manganese, copper, zinc, lead and cadmium with iron hydroxide in hydrothermal plumes (by the data of laboratory modeling). Oceanology 41, 502–507.

Schlesinger, W.H., Klein, E.M., Vengosh, A., 2017. Global biogeochemical cycle of vanadium. Proc. Natl. Acad. Sci. USA 114 (52), E11092–E11100.

Schmittner, A., Lund, D.C., 2015. Early deglacial Atlantic overturning decline and its role in atmospheric CO_2 rise inferred from carbon isotopes. Clim. Past 11 (2), 135–152.

Shimmield, G.B., Price, N.B., 1988. The scavenging of U, ^{230}Th and ^{231}Pa during pulsed hydrothermal activity at 20°S, East Pacific Rise. Geochim. Cosmochim. Acta 5, 669–677.

Speer, K.G., Rona, P.A., 1989. A model of an Atlantic and Pacific hydrothermal plume. J. Geophys. Res. 94 (C5), 6213–6220.

Speer, K.G., Maltrud, M.E., Thurnherr, A.M., 2003. A global view of dispersion on the Mid-Ocean Ridge. In: Halbach, P., Tunnicliffe, V., Hein, J. (Eds.), Energy and Mass Transfer in Marine Hydrothermal Systems. Dahlem University Press, Berlin, pp. 287–302.